

# Correlating magnetotransport and diamagnetism of $sp^2$ -bonded carbon networks through the metal-insulator transition

P. M. Vora,<sup>1</sup> P. Gopu,<sup>2</sup> M. Rosario-Canales,<sup>2</sup> C. R. Pérez,<sup>3</sup> Y. Gogotsi,<sup>3</sup> J. J. Santiago-Avilés,<sup>2</sup> and J. M. Kikkawa<sup>1,\*</sup>

<sup>1</sup>*Department of Physics and Astronomy, University of Pennsylvania, Philadelphia, Pennsylvania 19104, USA*

<sup>2</sup>*Department of Electrical and Systems Engineering, University of Pennsylvania, Philadelphia, Pennsylvania 19104, USA*

<sup>3</sup>*Department of Materials Science and Engineering, Drexel University, Philadelphia, Pennsylvania 19104, USA*

(Received 27 May 2011; revised manuscript received 27 September 2011; published 14 October 2011)

Titanium-carbide-derived carbons (TiC-CDCs) are porous  $sp^2$ -bonded networks synthesized by exposing TiC to chlorine gas at an elevated temperature. The latter “chlorination temperature” adjusts the size of the pores and the  $sp^2$ -bonded carbon domains within this material. We perform magnetoresistance, electronic transport, and superconducting quantum interference device magnetization measurements on TiC-CDC samples prepared at different chlorination temperatures. Transport reveals a metal-insulator transition where high (low) chlorination temperature samples are on the metallic (insulating) side of the transition. Magnetoresistance measurements are consistent with transport in the weak and strong localization regimes for metallic and insulating samples, respectively. Changes in diamagnetism, electronic transport, and magnetoresistance data across the metal-insulator transition are coordinated, suggesting that all three properties are controlled by a single parameter, likely the expansion of  $sp^2$ -bonded domains.

DOI: [10.1103/PhysRevB.84.155114](https://doi.org/10.1103/PhysRevB.84.155114)

PACS number(s): 81.05.uj, 72.80.Vp, 71.30.+h, 75.20.-g

## I. INTRODUCTION

Introducing disorder into  $sp^2$ -bonded carbon systems can lead to significant changes in their electronic and magnetic properties. Irradiation, doping, and finite-size effects may induce metal-insulator transitions,<sup>1–7</sup> anomalous magnetism,<sup>8–14</sup> and band gaps<sup>15–24</sup> in various forms of graphene and graphite. However, there is also a history of such effects occurring in networks composed of nano-sized domains of  $sp^2$ -bonded carbon. In particular, metal-insulator transitions have been found to occur in activated carbon fibers,<sup>25–28</sup> graphene oxide,<sup>6</sup> glassy and amorphous carbon materials,<sup>29–31</sup> fluorine-intercalated graphite fibers,<sup>32</sup> and carbon nanotube buckypapers.<sup>33</sup> The transition in many cases is induced by heat treatments, which adjust the size of the  $sp^2$ -bonded domains.<sup>25–31,33</sup> The effect of these structural modifications on the electronic and magnetic properties of the networks can be quantified through a variety of different experimental techniques. Magnetoresistance and electronic transport characterize how localization lengths behave on either side of the metal-insulator transition.<sup>28,32–34</sup> Raman and magnetization measurements have been used to evaluate the size of and disorder in  $sp^2$ -bonded domains by measuring the disorder-induced  $D$  peak and the number of unpaired spins.<sup>8,28,35</sup> However, there have not been measurements correlating behaviors across the metal-insulator transition with diamagnetism.

In this work, we correlate magnetoresistance, electronic transport, and diamagnetic susceptibility data across the metal-insulator transition in titanium-carbide-derived carbons (TiC-CDCs). These materials are synthesized by exposing TiC to chlorine gas at an elevated temperature, the “chlorination temperature.”<sup>36</sup> The resulting material is a three-dimensional porous network of  $sp^2$ -bonded carbon, where the porosity may be tuned with sub-Angstrom accuracy by adjusting the chlorination temperature.<sup>37–39</sup> TiC-CDCs, and carbide-derived carbons in general, hold great technological promise as a candidate material for supercapacitor electrodes.<sup>37</sup> The small pore size and large specific surface area in these materials

maximize the classical capacitance equation, yielding high energy densities.<sup>37–39</sup> While the synthesis procedures, structural properties, and capacitance of TiC-CDCs have been carefully studied,<sup>37–40</sup> their electronic transport mechanisms and magnetic properties remain largely unexplored. Here, we demonstrate that these systems transition from an insulating to metallic state with increasing chlorination temperature and that changes in the magnetoresistance, electronic transport, and diamagnetism data are coordinated.

## II. MATERIALS SYNTHESIS AND EXPERIMENTAL METHODS

### A. Materials synthesis and sample characteristics

Titanium-carbide-derived carbons (TiC-CDC) are synthesized from a carbide precursor, TiC, following the methods of Refs. 39 and 41. In summary, TiC powder (Alfa Aesar, 2  $\mu\text{m}$  average particle size) is placed in a quartz tube and heated in a furnace from room temperature to the chlorination temperature under Ar gas flow. The flow is then switched to  $\text{Cl}_2$  gas, which removes Ti atoms from TiC via the following reaction:



ideally leaving behind pure carbon.<sup>41</sup> Following this step, the carbon powders are treated with  $\text{H}_2$  gas for two hours at an elevated temperature.<sup>41</sup> This last step is intended to remove residual chlorine and metal chlorides from the powders. The  $\text{H}_2$  treatment temperature is usually less than or equal to the chlorination temperature to prevent further heat-induced annealing of the powder microstructure. The resulting material is a black powder whose constituents are porous carbon particles with high specific surface area and  $sp^2$ -bonded carbon domains. The porosity and  $sp^2$ -bonded domain size depend sensitively on the chlorination temperature.<sup>37–40</sup> Below 1000 °C, TiC-CDCs are predominantly composed of amorphous carbon.<sup>37</sup> At approximately 1000 °C, nonplanar

graphite becomes the primary component of the TiC-CDC structure, and at even higher temperatures, graphene sheets and graphite ribbons form.<sup>37</sup>

The samples used in this study are created from TiC-CDC powders chlorinated at 200, 300, 400, 600, 800, 900, 1000, 1100, and 1200 °C. Samples chlorinated at 200 and 300 °C are treated with H<sub>2</sub> gas at 200 and 300 °C, respectively, for two hours. All other samples are treated with H<sub>2</sub> gas at 600 °C for two hours, including the sample chlorinated at 400 °C. Since the H<sub>2</sub> treatment temperature exceeds the chlorination temperature for the 400 °C sample, there is a possibility of additional ordering.

The TiC-CDC powders are shaped into mats by the following procedure. A 60 wt% suspension of polytetrafluoroethylene (PTFE), purchased from Sigma Aldrich, is mixed with ethanol (EtOH). The TiC-CDC powder is mixed with EtOH separately, stirred for a few minutes, and then introduced to the PTFE-EtOH solution in a beaker on a hotplate. The solution is heated to evaporate the ethanol. The resulting mixture, 95 wt% TiC-CDC and 5 wt% PTFE suspension, is scraped onto a glass plate using a nonmagnetic spatula and shaped into a flat mat by repeatedly working it with the spatula as the ethanol evaporates. Small amounts of ethanol are used as necessary in the shaping process. The mats are then placed in a watch glass covered in aluminum foil inside a Lindberg-Blue laboratory vacuum oven (Model series: V0914C) at 92.5 °C.

From this point forward, samples will be referred to by their chlorination temperature alone, i.e., a sample chlorinated at 800 °C and treated with H<sub>2</sub> at 600 °C will be referred to as an “800 °C” sample.

### B. Experimental methods

For transport studies, the TiC-CDC mats are mounted on sapphire substrates using a thin layer of cryogenic high-vacuum grease (Apiezon N grease) to ensure good thermal contact between the mat and the substrate. The substrates are then mounted on a Quantum Design sample puck using the same grease and wired in a four-probe configuration using silver paint. Samples with high resistances are measured using a guarded triax two-probe measurement on a special home-built sample insert. The leakage resistance that limits these guarded measurements is 10<sup>15</sup> Ohms. The triax insert is then loaded into a Quantum Design Physical Property Measurement System (PPMS). Electrical measurements are made using a Keithley 237 Source-Measure Unit. The PPMS magnetic field points normal to the sample plane. Applied voltages are held constant during magnetic field and temperature sweeps, and chosen so that the sample current at 300 K is on the mA scale. IV data are linear at room temperature for the applied voltages, and we note that for insulating samples, the electric field is always much less than the threshold for nonlinear IV behavior in the variable range hopping (VRH) regime.<sup>32</sup> Magnetotransport studies are performed by measuring the sample resistance at constant voltage and temperature while the magnetic field is ramped between 9 and −9 tesla at a rate of 1.2 tesla/min. These magnetoresistance curves are acquired at 2, 3, 5, 8, 13, 20, and 32 K for most samples.

Magnetization studies are carried out in the Quantum Design Magnetic Property Measurement System (MPMS) superconducting quantum interference device (SQUID) magnetometer with the reciprocating sample option (RSO). TiC-CDC mats are folded and inserted into a clear straw, which is then loaded into the MPMS sample chamber. We note that the mats are held in place only by friction in the straw, not by placement in a gel capsule or small piece of straw as is commonly done. The background of the straw itself is below the noise floor of the SQUID (10<sup>−9</sup> emu), so our mounting procedure produces background-free measurements. Field sweeps are acquired at 300 and 2 K for all samples by performing RSO measurements at set magnetic fields between 7 and −7 tesla. Magnetization warming curves are measured by cooling the sample to 2 K and performing 7 tesla RSO measurements at fixed temperatures between 2 and 300 K defined on a roughly logarithmic scale.

## III. EXPERIMENTAL RESULTS AND ANALYSIS

### A. Electronic transport

Measurements of the temperature-dependent resistivity,  $\rho(T)$ , provide information on the electronic transport mechanisms in TiC-CDC mats synthesized at different chlorination temperatures. To characterize the conduction regimes more quantitatively, we calculate the reduced activation energy,<sup>27,33,42</sup>

$$W(T) = -\frac{d \ln \rho(T)}{d \ln T}, \quad (2)$$

where  $\rho(T)$  is the resistivity, for all samples in our study.  $W(T)$  may be used to differentiate between conduction regimes: if  $W$  increases (decreases) as  $T \rightarrow 0$  K, then the sample is on the insulating (metallic) side of the metal-insulator transition, whereas  $W$  is temperature independent in the critical regime.<sup>27,33,42</sup> Figure 1 presents  $W(T)$  for all samples in our study, with the inset showing the resistivities for a representative subset. Based on this classification scheme, most TiC-CDC mats in our study fall within the insulating regime. Exceptions are the 1100 and 1200 °C samples which lie in the critical and metallic regimes, respectively. We analyze  $\rho(T)$  of insulating samples in the context of VRH,<sup>43,44</sup>

$$\rho(T) = \rho_o \exp[(T_o/T)^p]. \quad (3)$$

For  $d$ -dimensional VRH,  $p = 1/(d + 1)$ ,  $k_B T_o = \beta/g(E_F)\xi^d$ ,  $g(E_F)$  is the  $d$ -dimensional density of states at the Fermi level,  $\beta$  is a numerically determined coefficient that has been calculated for each  $d$ , and  $\xi$  is the localization length.<sup>43–45</sup> The presence of strong Coulomb interactions results in a different type of hopping transport, Coulomb gap (CG) VRH, where Mott’s law is still valid but with slightly different parameters:  $p = 1/2$  and  $k_B T_o = 2.8e^2/\kappa\xi$ .<sup>43,44</sup> Here,  $\kappa$  is the effective dielectric constant and  $e$  is the electron charge. The  $W$  parameter in the VRH regime becomes

$$W(T) = p(T_o/T)^p \propto T^{-p}. \quad (4)$$

Figure 1 shows low-temperature power-law fits to  $W(T)$  for all samples. At chlorination temperatures of 1000 °C or less,  $p > 0$  and the samples are insulators. The specific values of  $p$  are variable, and may be compared to the predictions for

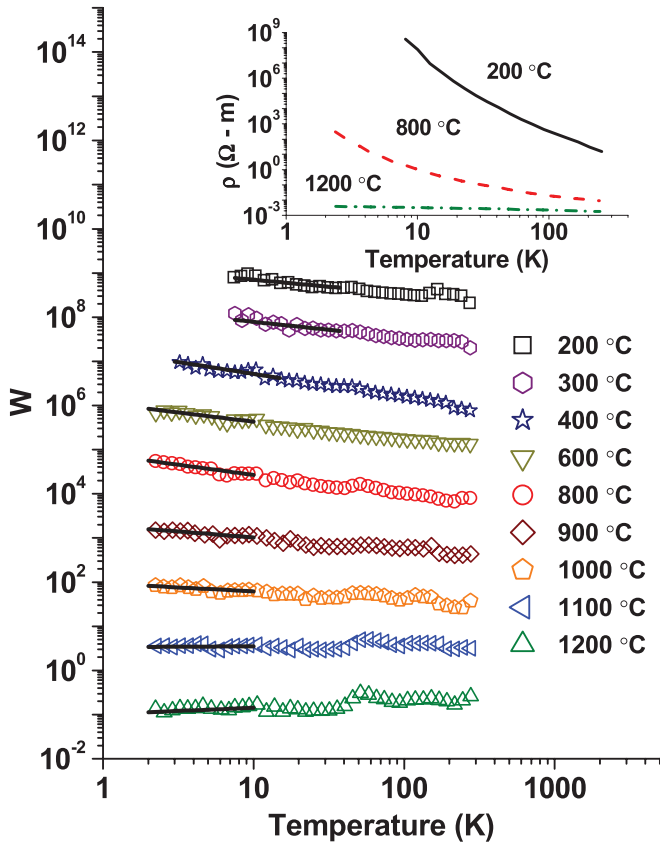


FIG. 1. (Color online) Reduced activation energy vs temperature for all samples. Legend indicates chlorination temperature. Curves are offset by multiples of 10 for clarity, leaving the 1200 °C data unscaled. Black lines are power-law fits to the low-temperature behavior. Inset: Temperature-dependent resistivity for the 200 (black solid line), 800 (red dashed line), and 1200 °C (green dash-dotted line) samples.

$d$ -dimensional and CG VRH (Fig. 2).<sup>43</sup> The microstructure of TiC-CDCs is dominated by amorphous carbon until the chlorination temperature approaches 1000 °C, at which point regions of nonplanar graphite appear.<sup>37</sup> The gradual ordering of the TiC-CDCs with chlorination temperature may lead to the promotion or suppression of different conduction mechanisms relative to each other and could explain the range of  $p$  values observed in Fig. 2.<sup>46</sup> For example, samples with a chlorination temperature of 800 °C or less have  $p$  values close to 1/2, suggesting that CG VRH may be important. We note that  $p = 1/2$  also occurs for one-dimensional (1D) VRH,<sup>43</sup> however, this mechanism is not likely considering that the underlying microstructure of our samples consists of  $sp^2$ -bonded domains that predominantly conduct in two dimensions and that these domains are arranged in a three-dimensional (3D) network.<sup>37</sup> The  $p$  values for the 900 and 1000 °C samples are close to values corresponding to VRH in 3D, however, the error bars are large enough that a definite assignment is not possible. We also fit  $W(T)$  data to a power law for the 1100 and 1200 °C samples at low temperatures (Fig. 1). While the exponent cannot be meaningfully interpreted in a VRH picture for these samples, it does serve as a measure of the transport regime and we include these values in Fig. 2. The resistivity of materials in the critical regime follows a power law,  $\rho(T) = aT^{-\beta}$ , and therefore

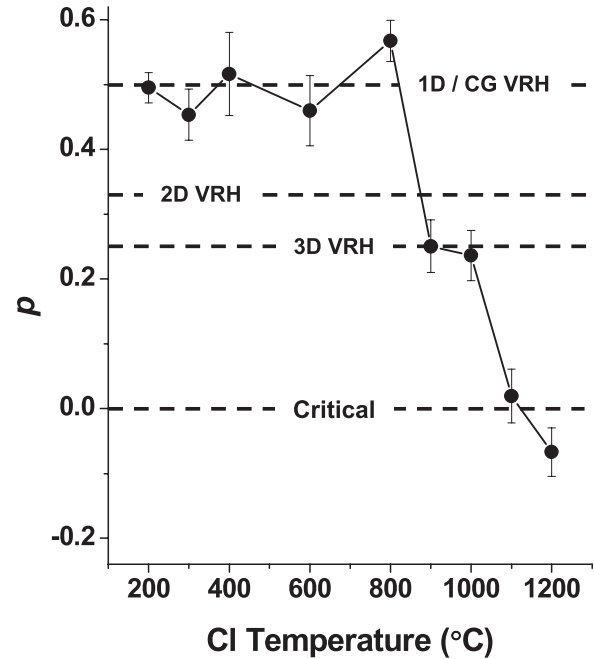


FIG. 2. The exponent  $p$  obtained from power-law fits of  $W(T)$  plotted vs chlorination temperature. Positive values correspond to insulating samples where  $p$  may be interpreted with VRH theory. The horizontal, dashed black lines label the  $p$  values for different types of VRH transport; where  $p = 1/(d + 1)$  and  $d$  is the dimension of VRH transport. In the case of CG VRH,  $p = 1/2$ . For samples lying on the boundary of the metal-insulator transition (critical regime),  $p = 0$  and is marked with a dashed black line. For metallic samples,  $p < 0$ .

$W = \beta$  is temperature independent.<sup>47</sup> Only the 1100 °C sample in our study exhibits such behavior.

TiC-CDCs synthesized at 1200 °C experience a high degree of graphitization,<sup>37,39</sup> making metallic conduction more likely. We find that only the 1200 °C sample exhibits a decreasing  $W(T)$  with decreasing temperature ( $p < 0$ ), indicating that it lies in the metallic regime.<sup>27,33,42</sup>

## B. Magnetoresistance studies: Connection to the metal-insulator transition

The sign and shape of magnetoresistance (MR) data are sensitive to the length scales and type of transport in the sample, making magnetoresistance a useful tool for studying metal-insulator transitions.<sup>27,33,42,43,48</sup> Magnetoresistance is defined by

$$\text{MR} = \frac{\rho(B, T) - \rho(0, T)}{\rho(0, T)} \times 100\%. \quad (5)$$

We acquire MR data for all samples over a range of different temperatures. The high resistance of the 200, 300, and 400 °C samples precluded the acquisition of MR at low temperatures due to instrumental limitations.

Magnetoresistance measurements serve as a sensitive probe of transport length scales in mesoscopic systems. In a wide variety of doped carbon nanotube systems, for example, a transition from positive to negative low-temperature MR has been observed as the system progresses from insulator

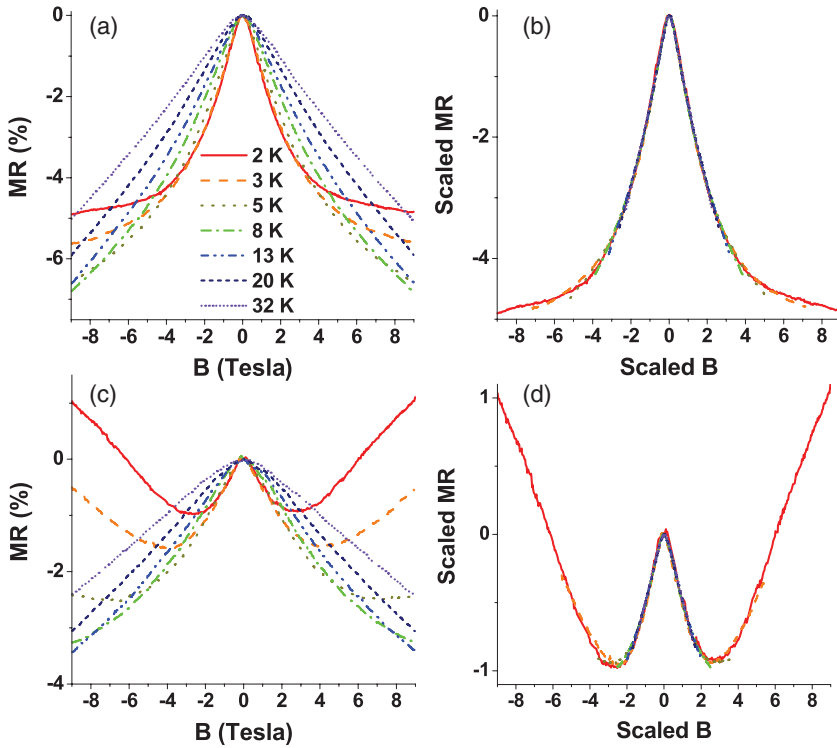


FIG. 3. (Color online) Magnetoresistance for TiC-CDC mats with chlorination temperatures of (a) 1200 and (c) 1100 °C. The legend labels the temperature at which each magnetoresistance curve was acquired. (b) and (d) contain the results of the MR scaling analysis described in the text for TiC-CDC mats synthesized at 1200 and 1100 °C, respectively.

to metal.<sup>33</sup> Similarly, for the 1200 °C metallic sample, all observed MR is negative [Fig. 3(a)] and the width of the MR curves decrease with decreasing temperature. Both of these behaviors are consistent with weak localization and we note that 2 and 3 K data show signs of saturation at high fields. The 1100 °C critical sample exhibits both positive and negative MR components at 2, 3, and 5 K [Fig. 3(c)], which are typically associated with magnetotransport in the strong and weak localization regimes<sup>33,43,48</sup> and suggest that these two mechanisms compete in the critical regime. This competition leads to MR minima at nonzero fields for data acquired at 2, 3, and 5 K. MR is negative at all other temperatures, although some positive background likely remains.

Prior studies of carbon nanotube buckypapers<sup>33</sup> found that weak localization magnetoresistance obeyed a universal form,  $Af(B/B_\phi)$ .  $A$  is the amplitude and  $B_\phi$  is the magnetic field that induces one magnetic flux quantum ( $\Phi_o$ ) through a weak localization scattering loop, commonly expressed as  $B_\phi = \Phi_o/4\pi L_\phi^2$ .<sup>33</sup> The approximate area of the loop circumscribed by the time-reversed paths is proportional to the square of the phase-coherence length,  $L_\phi^2$ .<sup>33</sup> We find that our data also obey a universal form, illustrated in Figs. 3(b) and 3(d), and from this scaling we obtain values of  $A$  and  $B_\phi$  by fitting our data at low fields with the 3D weak localization magnetoresistance model of Ref. 49. The magnetoconductivity in the 3D weak localization regime is<sup>49</sup>

$$\frac{\Delta\sigma_{3DWL}}{\sigma(0)} = k_1\sqrt{B}f_3\left(\frac{B}{B_\phi}\right), \quad (6)$$

where  $k_1 = e/[12\sqrt{\pi}\sigma(0)\Phi_o^{3/2}]$ ,  $\sigma(0) = 1/\rho(0)$  where  $\rho(0)$  is the zero-field resistivity, and  $f_3(x)$  is known as the Kawabata function.<sup>48,49</sup> At low fields,  $f_3(x) = x^{3/2}$  and Eq. (6)

simplifies to

$$\frac{\Delta\sigma_{3DWL}}{\sigma(0)} = k_1B^2B_\phi^{-3/2}. \quad (7)$$

By fitting the quadratic low-field behavior in Figs. 3(b) and 3(d), we obtain the temperature dependence of  $B_\phi$ , and therefore  $L_\phi^2$  (Fig. 4), in the metallic and critical regimes. The size of  $sp^2$ -bonded domains in the metallic sample are hundreds of square nanometers, quickly decreasing to tens of square nanometers as the chlorination temperature

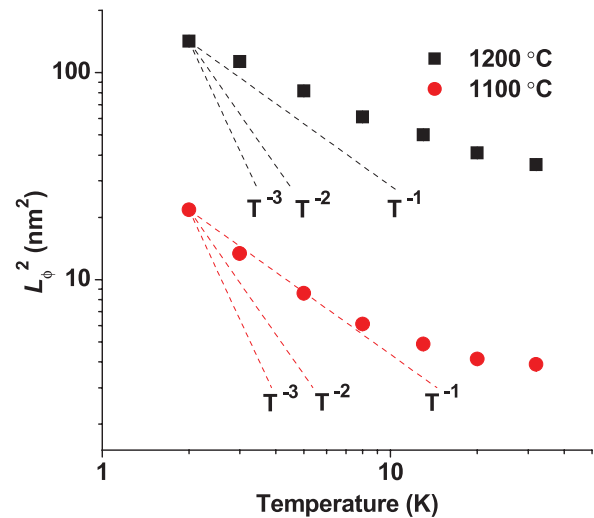


FIG. 4. (Color online)  $L_\phi^2$  vs temperature for TiC-CDC mats with chlorination temperatures of 1200 (black squares) and 1100 °C (red circles). Dashed lines show power-law predictions discussed in the text.

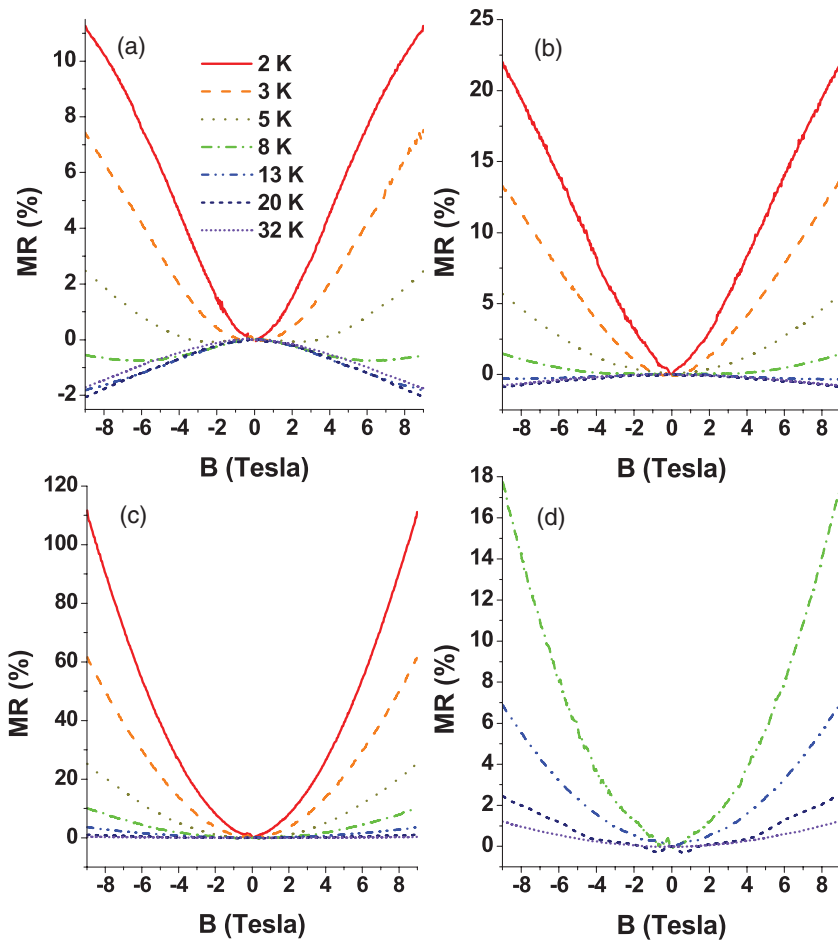


FIG. 5. (Color online) Magnetoresistance for TiC-CDC mats with chlorination temperatures of (a) 1000, (b) 900, (c) 800, and (d) 400 °C. The legend labels the temperature at which each magnetoresistance curve was acquired.

approaches 1000 °C.<sup>40</sup>  $L_{\phi}^2$  in the metallic and critical samples is comparable to or less than the domain size at all temperatures examined in this study, suggesting that phase-coherent transport is occurring within  $sp^2$ -bonded domains. Figure 4 shows predicted power-law behaviors for electron-phonon (el-ph) scattering ( $T^{-3}$ ), electron-electron (e-e) scattering in the clean limit ( $T^{-2}$ ), and e-e scattering close to the metal-insulator transition ( $T^{-1}$ ).<sup>42</sup> The prediction for e-e scattering in the dirty limit is  $T^{-1.5}$ , which is not shown.<sup>42</sup> The 1200 °C sample does not follow any of these predictions; however, the 1100 °C sample does approximate  $T^{-1}$  at low temperatures, as expected for a sample in the critical regime.

All other samples within our study lie in the insulating regime and we present the MR data for a select set in Fig. 5. Positive MR is expected for strongly localized systems and may originate from magnetic-field-induced shrinkage of localized wave functions, spin polarization, or a combination of these two effects.<sup>34,43</sup> Field-induced wave-function shrinkage reduces the overlap between localized electron wave functions and therefore the conductance. In contrast, spin polarization in a magnetic field suppresses some hopping pathways leading to an overall decrease in conductance. In both cases, the resulting MR is positive and quadratic at low fields.<sup>32,43</sup> Mechanisms also exist that produce negative MR in insulating systems. In analogy with weak localization, a system exhibiting VRH transport may experience a dephasing between distinct hopping paths that both traverse from one localized site to another under application of a magnetic field.<sup>50-52</sup> Under appropriate

conditions, this can result in a suppression of destructive interference between distinct hopping paths and a negative magnetoresistance, which is predicted to be either linear<sup>50,51</sup> or quadratic<sup>52</sup> at low fields. We also note that Zeeman shifts of localized electron states can produce negative, quadratic MR.<sup>32,53</sup>

Both the 1000 and 900 °C display positive MR at low temperatures that gradually transitions to negative MR as temperature increases. At intermediate temperatures, the MR data display minima at nonzero fields. These behaviors suggest a thermally driven competition between positive and negative MR mechanisms. MR is positive and displays no indications of saturation for samples with chlorination temperatures of 800 °C or lower, consistent with strong localization.<sup>42,43</sup> For samples with chlorination temperatures between 400 and 800 °C we find that most MR data exhibit quadratic behavior at low fields,  $MR = CB^2$ . While both spin and wave-function shrinkage effects lead to quadratic MR, the predicted temperature dependence of the quadratic MR coefficient,  $C$ , differs for these two mechanisms. In wave-function shrinkage MR,  $C$  is expected to follow a power law  $\sim T^{-3p}$ , where  $p$  is the VRH exponent in Eq. (3).<sup>43</sup>  $C$  thus scales as  $1/T^{3/2}$  for 1D or CG VRH,  $1/T$  for 2D VRH, and  $1/T^{3/4}$  for 3D VRH. Positive MR from spin results from Pauli exclusion and is a Boltzmann process parameterized by  $B/T$ , so that in this case  $C$  manifestly scales as  $1/T^2$ . For those data in Fig. 5 with unambiguous quadratic dependence, we found that  $C$  follows a  $1/T^2$  power law (Fig. 6), supporting a spin

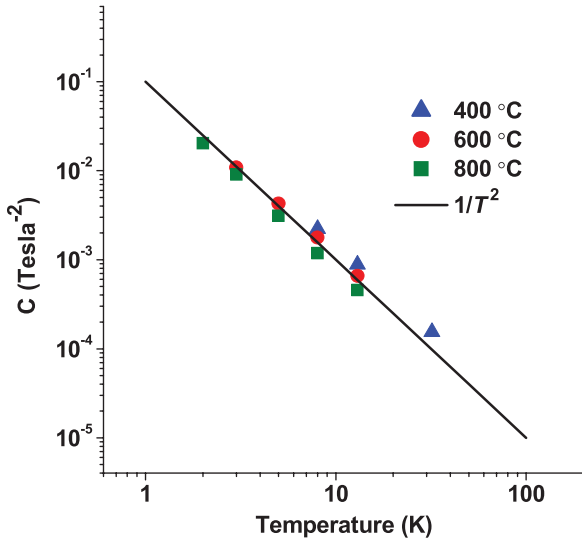


FIG. 6. (Color online) Coefficient of quadratic fits,  $C$  ( $\text{tesla}^{-2}$ ), vs temperature for TiC-CDC mats with chlorination temperatures of 400 (blue triangles), 600 (red circles), and 800 °C (green squares). The data follow an approximately  $1/T^2$  power law (black line).

MR mechanism. It is worth noting that similar exponents have been reported in studies of poly (*p*-phenylenevinylene)<sup>54</sup> and activated carbon fibers,<sup>34</sup> although spin MR was not assigned. The temperature dependence of  $C$  may help distinguish between spin polarization (isotropic) and wave-function shrinkage (anisotropic) effects, particularly in systems such as ours where anisotropic MR measurements are problematic due to the randomly oriented sample microstructure.

**C. Magnetization studies**

Diamagnetism is an informative probe of carrier delocalization in  $sp^2$ -bonded carbons. As  $C_6$  hexagons are assembled into large molecules, diamagnetism first grows in direct proportion to the number of rings.<sup>55,56</sup> Ring currents are additive in this regime, canceling at every shared edge and leaving a single persistent current around the edge of the molecule.<sup>56</sup> The diamagnetic moment is then simply proportional to the area of the molecule. Therefore, provided that the metal-insulator transition in TiC-CDC mats arises from gradual nucleation of large  $sp^2$ -bonded domains, we should expect the diamagnetic susceptibility to increase with chlorination temperature. We carried out studies of the magnetization,  $M$ , as a function of  $B$  and  $T$  in all samples except the 300 and 200 °C in an effort to observe this effect. Results for field sweeps at 300 and 2 K are shown in Figs. 7(a) and 7(b), respectively, where we have normalized the magnetization by the molar mass of the TiC-CDC mat. At 300 K, we observe a strong diamagnetic contribution to the total moment, evidenced by the negative slope of the field-sweep curves at high field for most samples. Some samples exhibit a small ferromagnetic contribution near  $B = 0$  tesla, most likely due to impurities introduced during synthesis. The 2 K field-sweep data reveal a significant paramagnetic contribution, which dominates at low temperatures (particularly in the 800 °C sample).

To extract the 300 K diamagnetic susceptibility for each sample, we first estimate the small ferromagnetic contribution using linear fits to the positive and negative low-field regions (0.5–1.5 tesla) of the 300 K field sweeps [Fig. 7(a)]. Specifically, we associate the ferromagnetic moment as the zero-field intercepts of these fits. To identify the paramagnetic contribution, we record magnetization upon warming from 2 to 300 K in a relatively large field of 7 tesla, which minimizes

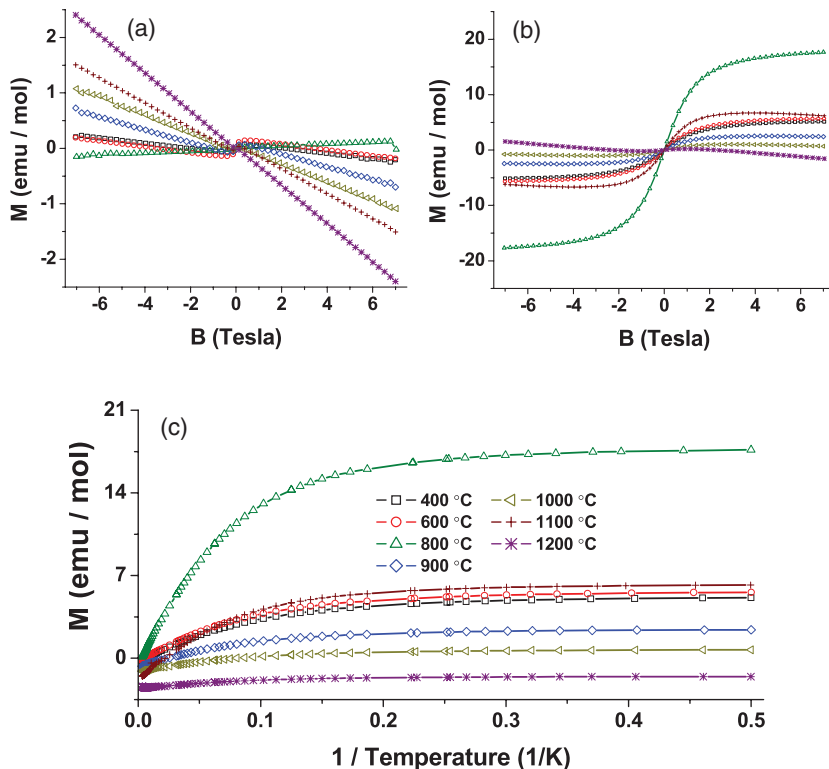


FIG. 7. (Color online) Magnetization  $M$  vs  $B$  field-sweep curves for TiC-CDC mats with chlorination temperatures greater than 300 °C acquired at (a) 300 and (b) 2 K. In (c), we plot  $M$  vs  $1/T$ . The chlorination temperatures of the TiC-CDC mats are summarized in the legend of (c).

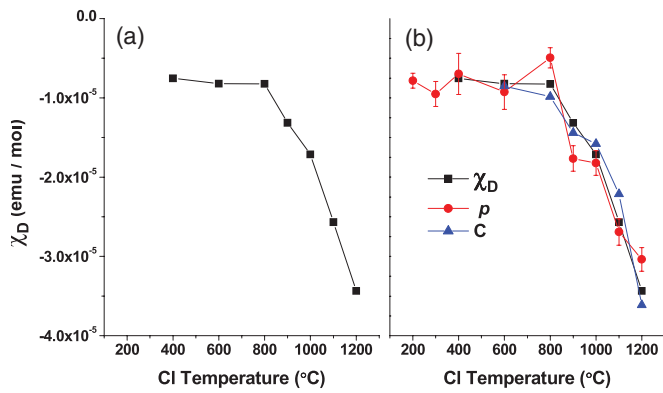


FIG. 8. (Color online) (a) Diamagnetic susceptibility  $\chi_D$  plotted vs chlorination temperature. In (b), we have collapsed the VRH exponent  $p$  (red circles), the quadratic MR coefficient  $C$  (blue triangles), and  $\chi_D$  (black squares) data onto each other by scaling and offsetting the curves. The quadratic MR coefficients were determined from 3 K MR data.

the relative ferromagnetic contribution and yet produces paramagnetism linear in  $B/T$  at the highest temperatures studied here [Figs. 7(a) and 7(c)]. The room-temperature diamagnetic susceptibility is then obtained by extrapolating the magnetization at zero inverse temperature [ $y$  intercept of Fig. 7(c)] and subsequently applying the small ferromagnetic correction discussed above. The results, presented in Fig. 8(a), demonstrate that the diamagnetic susceptibility increases with increasing chlorination temperature, strongly supporting the idea that the metal-insulator transition in TiC-CDC mats is driven by the growth of  $sp^2$ -domains, whose size is controlled by the chlorination temperature.

Our study thus establishes coordinated changes in resistivity, MR, and diamagnetism in these samples. Theoretical discussions almost necessarily treat strong and weak localization regimes as distinct, but here we show that a continuous transition between the two can be meaningfully parameterized by the diamagnetic susceptibility. In Fig. 8(b), we have collapsed the chlorination temperature dependence of (i) the hopping exponent  $p$ , (ii) the low-field, low-temperature quadratic MR coefficient  $C$ , and (iii) the 300 K diamagnetic susceptibility  $\chi_D$  onto each other by scaling and offsetting the curves. The overlap of these data demonstrates a striking

correlation between these quantities, suggesting that all three are controlled by a single basic property. The dependence on chlorination temperature suggests the likely culprit is an expansion of  $sp^2$ -bonded domains with increasing chlorination temperature.

#### IV. CONCLUSION

In this study, we examined diamagnetism, magnetoresistance, and electronic transport in TiC-CDC mats synthesized at different chlorination temperatures. Our results point to a metal-insulator transition occurring near a chlorination temperature of 1100°C. Samples with lower (higher) chlorination temperatures are on the insulating (metallic) side of the transition. We analyze magnetoresistance and electronic transport data in the strong and weak localization regimes for insulating and metallic samples, respectively. SQUID magnetization measurements of diamagnetism demonstrate that TiC-CDCs become increasingly diamagnetic with increasing chlorination temperature, pointing to the expansion of  $sp^2$ -bonded domains as driving the metal-insulator transition. We correlate changes in the diamagnetic susceptibility  $\chi_D$ , the VRH exponent  $p$ , and the quadratic MR coefficient  $C$  with chlorination temperature, finding that all three are coordinated and obey a similar functional form. The growth of  $sp^2$ -bonded domains drives the changes of these three different, but related, quantities. In closing, we comment that the strong and weak localization regimes are sometimes treated independently. The coordinated, continuous changes in diamagnetism, magnetoresistance, and electronic transport observed here imply that for metal-insulator transitions in  $sp^2$ -bonded carbons, one can construct a single theory encompassing both sides of the transition where the only relevant parameter is the  $sp^2$ -bonded domain size.

#### ACKNOWLEDGMENTS

J. M. K and PMV acknowledge the support of NSF Grant Nos. DMR-0907266 and MRSEC DMR-05-20020. C. R. P acknowledges the support of NSF IGERT Grant No. (DGE-0654313) and the GK12 fellowship program. P. G, M. R, and J. J. S were partially supported by the Nano/Bio Interface Center through the National Science Foundation Grant No. NSEC DMR08-32802.

\*Author to whom correspondence should be addressed: kikkawa@physics.upenn.edu

<sup>1</sup>D. C. Elias, R. R. Nair, T. M. G. Mohiuddin, S. V. Morozov, P. Blake, M. P. Halsall, A. C. Ferrari, D. W. Boukhvalov, M. I. Katsnelson, A. K. Geim, and K. S. Novoselov, *Science* **323**, 610 (2009).

<sup>2</sup>S. Adam, S. Cho, M. S. Fuhrer, and S. Das Sarma, *Phys. Rev. Lett.* **101**, 046404 (2008).

<sup>3</sup>A. Bostwick, J. L. McChesney, K. V. Emtsev, T. Seyller, K. Horn, S. D. Kevan, and E. Rotenberg, *Phys. Rev. Lett.* **103**, 056404 (2009).

<sup>4</sup>S. Y. Zhou, D. A. Siegel, A. V. Fedorov, and A. Lanzara, *Phys. Rev. Lett.* **101**, 086402 (2008).

<sup>5</sup>J.-H. Chen, W. G. Cullen, C. Jang, M. S. Fuhrer, and E. D. Williams, *Phys. Rev. Lett.* **102**, 236805 (2009).

<sup>6</sup>G. Eda, C. Mattevi, H. Yamaguchi, H. Kim, and M. Chhowalla, *J. Phys. Chem. C* **113**, 15768 (2009).

<sup>7</sup>N. Leconte, J. Moser, P. Ordejón, H. Tao, A. Lherbier, A. Bachtold, F. Alsina, C. M. Sotomayor Torres, J.-C. Charlier, and S. Roche, *ACS Nano* **4**, 4033 (2010).

<sup>8</sup>Y. Shibayama, H. Sato, T. Enoki, and M. Endo, *Phys. Rev. Lett.* **84**, 1744 (2000).

- <sup>9</sup>P. Esquinazi, D. Spemann, R. Hohne, A. Setzer, K.-H. Han, and T. Butz, *Phys. Rev. Lett.* **91**, 227201 (2003).
- <sup>10</sup>P. Esquinazi, R. Hohne, K.-H. Han, A. Setzer, D. Spemann, and T. Butz, *Carbon* **42**, 1213 (2004).
- <sup>11</sup>H. Ohldag, T. Tylliszczak, R. Höhne, D. Spemann, P. Esquinazi, M. Ungureanu, and T. Butz, *Phys. Rev. Lett.* **98**, 187204 (2007).
- <sup>12</sup>T. Enoki and K. Takai, *Solid State Commun.* **149**, 1144 (2009).
- <sup>13</sup>J. Cervenka, M. I. Katsnelson, and C. F. J. Flipse, *Nature Phys.* **5**, 840 (2009).
- <sup>14</sup>M. M. Ugeda, I. Brihuega, F. Guinea, and J. M. Gómez-Rodríguez, *Phys. Rev. Lett.* **104**, 096804 (2010).
- <sup>15</sup>M. Y. Han, B. Ozyilmaz, Y. Zhang, and P. Kim, *Phys. Rev. Lett.* **98**, 206805 (2007).
- <sup>16</sup>Z. Chen, Y.-M. Lin, M. Rooks, and P. Avouris, *Physica E* **40**, 228 (2007).
- <sup>17</sup>X. Li, X. Wang, L. Zhang, S. Lee, and H. Dai, *Science* **319**, 1229 (2008).
- <sup>18</sup>J. Bai, X. Zhong, S. Jiang, Y. Huang, and X. Duan, *Nature Nano.* **5**, 190 (2010).
- <sup>19</sup>S.-H. Cheng, K. Zou, F. Okino, H. R. Gutierrez, A. Gupta, N. Shen, P. C. Eklund, J. O. Sofo, and J. Zhu, *Phys. Rev. B* **81**, 205435 (2010).
- <sup>20</sup>Z. Luo, P. Vora, E. Mele, A. Johnson, and J. Kikkawa, *Appl. Phys. Lett.* **94**, 111909 (2009).
- <sup>21</sup>T. Gokus, R. R. Nair, A. Bonetti, M. Boehmler, A. Lombardo, K. S. Novoselov, A. K. Geim, A. C. Ferrari, and A. Hartschuh, *ACS Nano* **3**, 3963 (2009).
- <sup>22</sup>X. Sun, Z. Liu, K. Welsher, J. T. Robinson, A. Goodwin, S. Zaric, and H. Dai, *Nano Res.* **1**, 203 (2008).
- <sup>23</sup>G. Eda, Y.-Y. Lin, C. Mattevi, H. Yamaguchi, H.-A. Chen, I.-S. Chen, C.-W. Chen, and M. Chhowalla, *Adv. Mater.* **22**, 505 (2010).
- <sup>24</sup>X. Yan, X. Cui, B. Li, and L.-s. Li, *Nano Lett.* **10**, 1869 (2010).
- <sup>25</sup>K. Kuriyama and M. S. Dresselhaus, *J. Mater. Res.* **7**, 940 (1992).
- <sup>26</sup>K. Kuriyama, *Phys. Rev. B* **47**, 12415 (1993).
- <sup>27</sup>A. W. P. Fung, M. S. Dresselhaus, and M. Endo, *Phys. Rev. B* **48**, 14953 (1993).
- <sup>28</sup>Y. Shibayama, H. Sato, T. Enoki, X.-X. Bi, M. S. Dresselhaus, and M. Endo, *J. Phys. Soc. Jpn.* **69**, 754 (2000).
- <sup>29</sup>V. Prasad and S. Subramanyam, *Physica B* **369**, 168 (2005).
- <sup>30</sup>V. Prasad, *Solid State Commun.* **145**, 186 (2008).
- <sup>31</sup>R. R. Saxena and R. H. Bragg, *J. Non-Cryst. Solids* **28**, 45 (1978).
- <sup>32</sup>S. L. di Vittorio, M. S. Dresselhaus, M. Endo, and T. Nakajima, *Phys. Rev. B* **43**, 12304 (1991).
- <sup>33</sup>J. Vavro, J. M. Kikkawa, and J. E. Fischer, *Phys. Rev. B* **71**, 155410 (2005).
- <sup>34</sup>A. W. P. Fung, Z. H. Wang, M. S. Dresselhaus, G. Dresselhaus, R. W. Pekala, and M. Endo, *Phys. Rev. B* **49**, 17325 (1994).
- <sup>35</sup>G. A. M. Reynolds, A. W. P. Fung, Z. H. Wang, M. S. Dresselhaus, and R. W. Pekala, *Phys. Rev. B* **50**, 18590 (1994).
- <sup>36</sup>M. Arulepp, J. Leis, M. Lätt, F. Miller, K. Rumma, E. Lust, and A. Burke, *J. Power Sources* **162**, 1460 (2006).
- <sup>37</sup>V. Presser, M. Heon, and Y. Gogotsi, *Adv. Funct. Mater.* **21**, 810 (2011).
- <sup>38</sup>J. Chmiola, C. Largeot, P.-L. Taberna, P. Simon, and Y. Gogotsi, *Science* **328**, 480 (2010).
- <sup>39</sup>J. Chmiola, G. Yushin, R. Dash, and Y. Gogotsi, *J. Power Sources* **158**, 765 (2006).
- <sup>40</sup>J. Palmer, A. Llobet, S.-H. Yeon, J. Fischer, Y. Shi, Y. Gogotsi, and K. Gubbins, *Carbon* **48**, 1116 (2010).
- <sup>41</sup>C. Portet, D. Kazachkin, S. Osswald, Y. Gogotsi, and E. Borguet, *Thermochim. Acta* **497**, 137 (2010).
- <sup>42</sup>R. Menon, C. O. Yoon, D. Moses, A. J. Heeger, and Y. Cao, *Phys. Rev. B* **48**, 17685 (1993).
- <sup>43</sup>B. I. Shklovskii and A. L. Efros, *Electronic Properties of Doped Semiconductors* (Springer Verlag, Berlin, 1984).
- <sup>44</sup>N. F. Mott, *Metal-Insulator Transitions* (Taylor & Francis, London, 1990).
- <sup>45</sup>N. F. Mott, *Conduction in Non-Crystalline Materials* (Oxford University Press, Oxford, 1987).
- <sup>46</sup>Y. Meir, *Phys. Rev. Lett.* **77**, 5265 (1996).
- <sup>47</sup>A. I. Larkin and D. E. Khmel'nitskii, *Sov. Phys. Usp.* **25**, 185 (1982).
- <sup>48</sup>P. A. Lee and T. V. Ramakrishnan, *Rev. Mod. Phys.* **57**, 287 (1985).
- <sup>49</sup>A. Kawabata, *Solid State Commun.* **34**, 431 (1980).
- <sup>50</sup>V. Nguen, B. Spivak, and B. Shklovskii, *Sov. Phys. JETP* **62**, 1021 (1985).
- <sup>51</sup>W. Schirmacher, *Phys. Rev. B* **41**, 2461 (1990).
- <sup>52</sup>U. Sivan, O. Entin-Wohlman, and Y. Imry, *Phys. Rev. Lett.* **60**, 1566 (1988).
- <sup>53</sup>H. Fukuyama and K. Yoshida, *J. Phys. Soc. Jpn.* **46**, 102 (1979).
- <sup>54</sup>M. Ahlskog, R. Menon, A. J. Heeger, T. Noguchi, and T. Ohnishi, *Phys. Rev. B* **55**, 6777 (1997).
- <sup>55</sup>S. Mrozowski, *Phys. Rev.* **85**, 609 (1952).
- <sup>56</sup>H. Akamatu, H. Inokuchi, and T. Handa, *Nature (London)* **168**, 520 (1951).